symmetry

MDPI

Article

Experimental and Numerical Studies of the Heat Transfer in Thin-Walled Rectangular Tubes under Fire

Renáta-Ildikó Száva [1], Betti Bolló [2], Péter Bencs [2], Károly Jármai [2], Ioan Száva [1,*], Gabriel Popa [1], Zsolt Asztalos [1] and Sorin Vlase [1,3,*]

[1] Department of Mechanical Engineering, Transilvania University of Brașov, B-dul Eroilor 20, 500036 Brașov, Romania
[2] Department of Mechanics, University of Miskolc, 3515 Miskolc, Hungary
[3] Romanian Academy of Technical Sciences, 010071 Bucharest, Romania
* Correspondence: eet@unitbv.ro (I.S.); svlase@unitbv.ro (S.V.); Tel.: +40-722-643020 (S.V.)

Abstract: The paper studies, experimentally and numerically, the fire behavior of some structural elements of symmetric-tubular (rectangular in this study) shapes using modern dimensional analysis (MDA). A model at a certain scale of the real prototype is analyzed in order to obtain its response in case of fires. Experimental measurements are performed on a 1:10 scale model of a real support pillar and compared with the results of the numerical simulation. The obtained results can have useful applications in engineering practice, allowing fast obtaining of results with minimal costs.

Keywords: modern dimensional analysis; symmetrical tubes; fire; numerical experiment

Citation: Száva, R.-I.; Bolló, B.; Bencs, P.; Jármai, K.; Száva, I.; Popa, G.; Asztalos, Z.; Vlase, S. Experimental and Numerical Studies of the Heat Transfer in Thin-Walled Rectangular Tubes under Fire. *Symmetry* **2022**, *14*, 1781. https://doi.org/10.3390/sym14091781

Academic Editor: Victor A. Eremeyev

Received: 20 July 2022
Accepted: 23 August 2022
Published: 26 August 2022

1. Introduction

In the analysis of large structures, modern dimensional analysis (*MDA*) has lately become frequently used [1–3]. Historically, the correlation between the behavior of the model and the prototype has been gradually studied, using different mathematical methods, such as geometric analogy (*GA*), theory of similarity (*TS*), and classical dimensional analysis (*CDA*) [4–6]. Although the *CDA* allows a comprehensive approach, due to its rather cumbersome methodology, it has not become sufficiently widespread among researchers. Properties of symmetry, as it is presented in this study, make it possible to reduce the number of the significant parameters that are necessary to take into account. Here are some of the shortcomings of the method, presented in [7–9]:

- Model Law (*ML*), which includes the correlations of model behavior and prototype through dimensionless variables π_j, $j = 1, 2, \ldots, n$, and requires a skill obtained from previous applications;
- This protocol is non-unitary, requiring both deep knowledge in the field from the one who wants to apply it, and a certain ingenuity in separating and grouping the variables involved in describing the phenomenon in order to obtain the desired dimensionless variables;
- The protocol is not only difficult, but also precarious, because only in relatively simple cases does it allow us to obtain all the desired dimensionless variables (which would serve us to the complete description of the model–prototype correlation);
- The protocol also involves significant mathematical knowledge, which ensures the correct formulation of laws that describe as accurately as possible the pursued phenomenon (for example, heat transfer).

As a result, the *CDA* had and has limited applicability. With the development of *MDA*, these shortcomings were solved, and the method became unitary, efficient, and easy, and, last but not least, it allowed the complete obtaining of the Model Law (*ML*), including all dimensionless variables, which describe the correlation between model and

prototype [10,11]. Applications of the method are found in numerous works, i.e., [12–16]. The obtaining of the *ML* elements will be briefly illustrated in Appendix A based on the results presented in the works [10,11,17].

In their contribution, the authors of this paper briefly presented the method called MDA in order to study and to show its net advantages compared to other methods that use the behavior of the model in viewing the predicted behavior of the prototype. Next, reference is made only to the particularities of applying this MDA method to bars with tubular–rectangular sections. New results concerning the MDA are presented in [18–22]. The results of the experiments obtained in this paper come to confirm the validity of the applied method.

In [9], the authors presented the applicability of MDA to heat transfer in bars and bar structures of circular sections. An analysis of the straight bars of rectangular–tubular sections is made in [23], where the *ML* is deduced for this type of heat transfer. A comparison made in [24–26] proves that for similar results, the time and efforts made using MDA are significantly reduced compared to where experimental determinations would be made. Other new results concerning the method and new application are presented in [27–30].

In the paper, experimentally and numerically, the fire behavior of some structural elements of a symmetric-tubular shape using MDA is presented. A model at a certain scale of the real prototype is analyzed in order to obtain its response in case of fires. There are experimental measurements performed on a 1:10 scale model of a real support pillar, and these are compared with the results of the numerical simulation. This allows the designers to obtain results in a short time and with minimal costs.

2. Materials and Methods

In a normal case, the approach to the problem of fire resistance of structural elements is conducted either in specially designed furnaces or in enclosures of considerable size, and therefore at a particularly high cost.

In order to substantially reduce material costs and working time, the authors proceeded from the results of thorough investigations carried out by [31] on the size of the heat transfer coefficient (thermal conductivity) to a thermal insulation material often used in the protection of fire (intumescent solvent-based paint type: Interchar 404, from International Marine and Protective Coatings).

Regarding this, one paper [31] examines two ways of heating the resized structural element (a steel bar), namely:

- Direct heating of the structural element covered with intumescent paint, i.e., when the thermal flux was applied from the outside to the protected element, resulting in $\lambda = 0.1089 \frac{W}{m \cdot K} = 0.1089 \frac{W}{m \cdot ^\circ C}$, a value specified in the technical data sheet of the paint;
- Reverse heating, when the thermal flux was applied (through an electric current) from inside the structural element to the outside, thus obtaining $\lambda = 0.1102 \frac{W}{m \cdot K} = 0.1102 \frac{W}{m \cdot ^\circ C}$, a difference of approximately 1%, which is highly acceptable considering the fact that these investigations did not have metrological conditions.

Consequently, even if at first glance the result seems to be a little curious, the thermal flux direction does not have a special significance in the behavior of the thermal insulation layer, respectively on the parameters of the thermal flux propagation, obtaining practically identical effects.

However, from the point of view of the necessary equipment, the effects are significant. Compared to direct heating, where the equipment has the disadvantages mentioned before, in the case of reverse heating, the equipment becomes very simple and cheap, with a practically 100 % reproducibility of the effects of fires or simply the pursuit of the heat flux propagation in a structural element.

Heating (reverse) with the help of electric power sources, if the control system is efficient, will lead to significant savings in the involved equipment and material costs, staff,

and, not least, fire protection conditions, which must be fulfilled in the case of open fire sources, applied to direct heating.

This simple and safe way of testing will open new perspectives, both in the field of testing intumescent paints and in the propagation of heat flux along structural elements made of steel.

In this paper, the authors opted for the reverse heating method where both the heating source and the investigation protocol were based on this method. In the present paper, the authors started from the experimental study of the 1:10 scale model of a real 5 m high support pillar, provided with four beams with a length of 4 m, from a domestic industrial hall, with the dimensions of 20×25 m^2.

The column, being of a tubular-square shape, and the adapted model also presented these characteristics, shown in Figure 1.

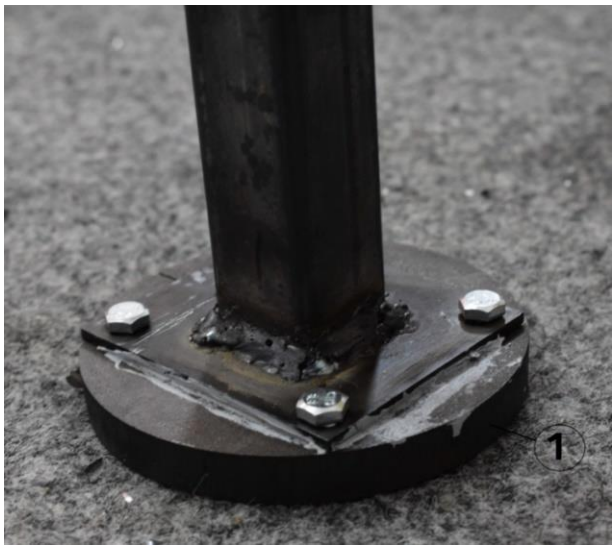

Figure 1. Detail with the lower area of the pillar model.

The dimensions of the frame column are $0.030 \times 0.030 \times 0.0015$ m, the height is 0.5 m and the dimensions of the beam are 0.010×0.0015 m with a length of 0.2 m.

In order to eliminate the undesirable influence of some accidental current of air from our lab and taking the reduced thermal inertia of this column into consideration, the column was foreseen with a 0.025 m-thick heat-insulation open cylinder, with a 0.45 m diameter and 0.65 m height (see Figure 2). The radius of this heat-insulation cylinder is comparable (at the reduced scale of 1:10) with the half-distance between the columns. A steel cylinder with a diameter of 0.105 m and a height of 0.015 m is fixed at the bottom of the column, which provides the electric heating. In advance, on the bottom of the column, a $0.080 \times 0.080 \times 0.003$ m steel plate was welded in order to make the mounting of the above-mentioned steel cylinder (Figure 1) easier. The temperature at the bottom of the support column is known from the heating performance and measurements, so the circular heating was not modelled. At the bottom of the column, a constant nominal temperature was prescribed (T = 100; 200; 300; 350; 400; 500 °C).

To monitor the thermal regimes inside the column, three PT 100-402 type thermal resistors were fixed on a thin steel rod, with 0.150 m-long terminals and a measuring range of $(-70 \ldots +500\ ^\circ\mathrm{C})$, at well-defined distances from the base of the column (at 0.165 m, 0.245 m and 0.305 m). It can be observed that the subassembly was mounted inside the column (Figures 2 and 3).

Additionally, to monitor the ambient temperature thus delimited by the thermal protection cylinder, another PT was fixed on a thin steel support at a distance of 0.060 m from the top of the column (Figures 2 and 3a).

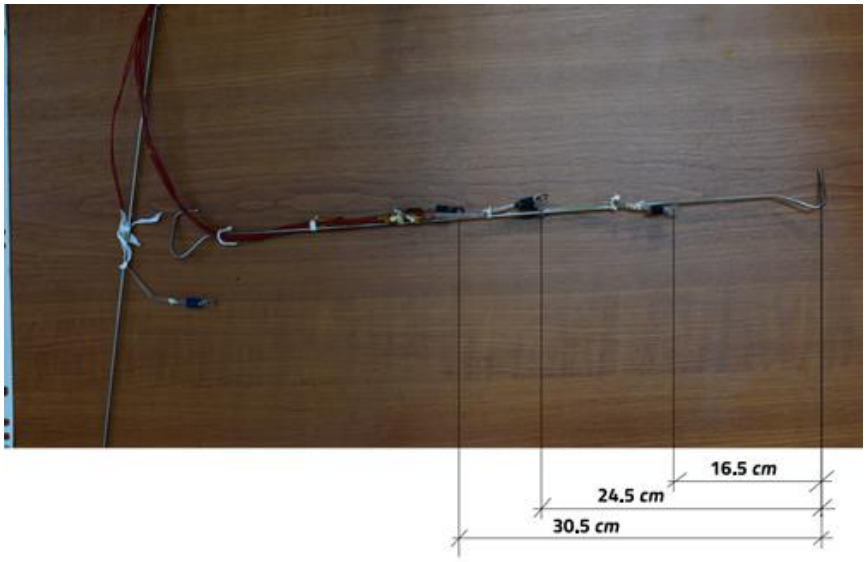

Figure 2. Set of PTs for monitoring the temperature of the air inside the beam and the environment.

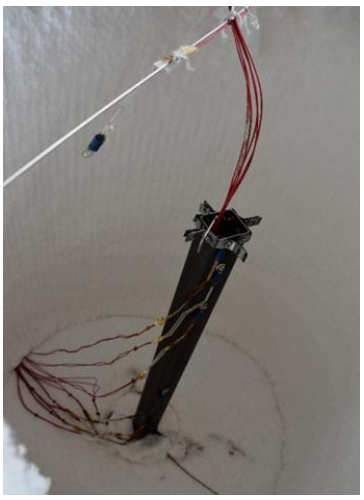

(**a**) Experimental setup. One column

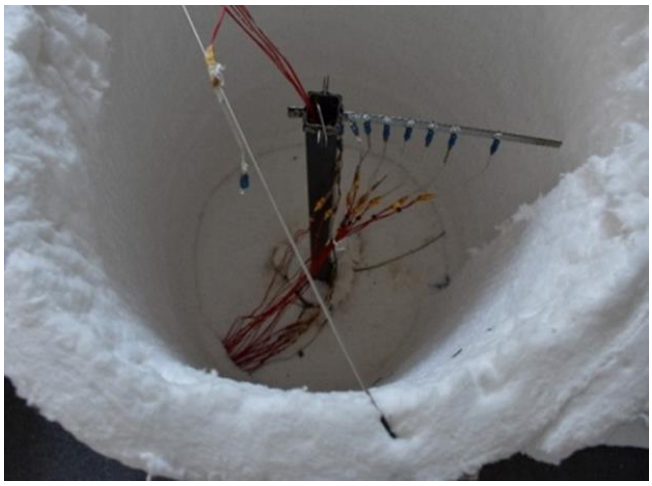

(**b**) One column with one bar

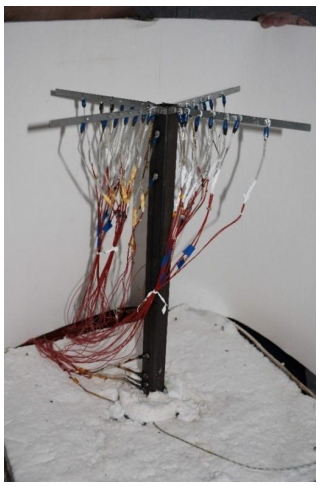

(**c**) One column and four bars

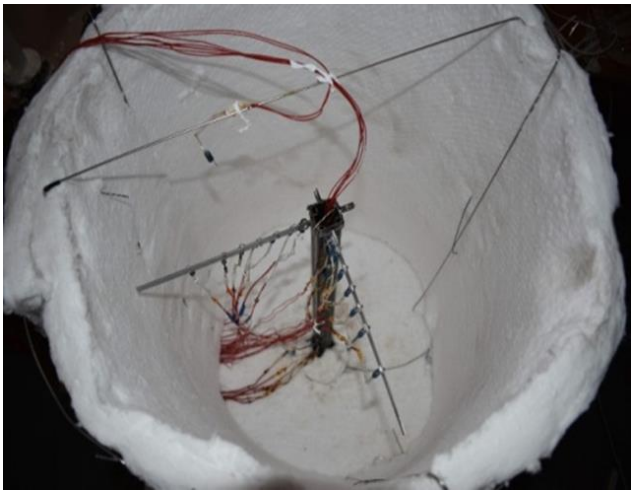

(**d**) One column and two bars

Figure 3. Stages of mounting the PT heat resistors on the pillar, indoors and environment, respectively, on the four beams [12].

Figure 3 shows the single pole with the PTs mounted, as well as the set of PTs intended for monitoring the temperature inside the pole in three places (on its height), and the ambient environment, with the PT mounted on the crossbar of wire located above the pole; in Figure 3b, it is the first beam installed, in Figure 3c it is all the beams installed, and in Figure 3d, it is shown as a detail with the post and two beams.

The trusses were made of flat steel with dimensions of 0.010 × 0.0015 m and a length of 0.200 m, in compliance with the law of the model, deduced and validated in [13], especially with reference to the Shape Factor $\varsigma \left[\frac{1}{m}\right]$ related to the real beams and the model [10,11]. The arrangement of the locations of the PTs fixed on the beams is shown in Figure 4. Here, the distances are presented in mm.

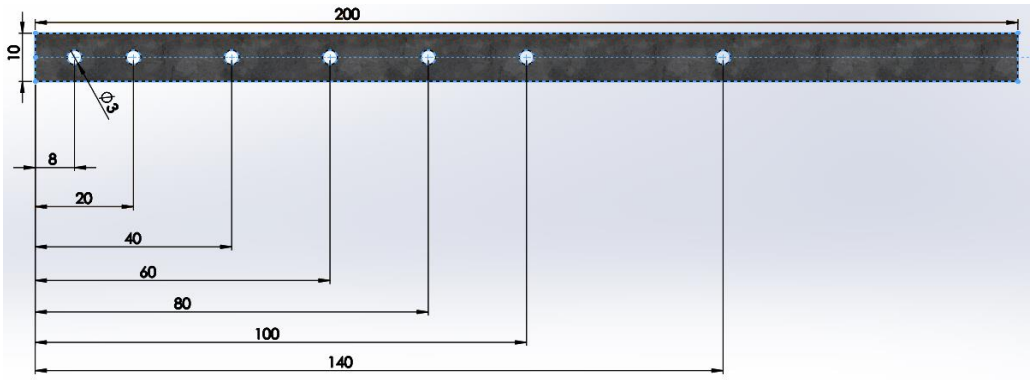

Figure 4. The positions of the PTs on the beam model, starting from its fixing section on the pillar.

At the base of the pole, in the welding area, a type K thermocouple was mounted to control the nominal entering temperature. Nine PTs were fixed along the length of the column in the following order z (1) = 0.015 m, z (2) = 0.030 m, z (3) = 0.045 m, z (4) = 0.060 m, z (5) = 0.100 m, z (6) = 0.200 m, z (7) = 0.400 m, and z (8) = 0.460 m and, at the upper end of the pole, at z (9) = 0,495 m, so their dimensions were starting from the base of zGy plan.

In addition, in order to be able to properly place this column (together with its cylindrical support) on the laying area of the support in the form of a pyramid triangle on the stand, an intermediate support (a stainless steel plate with dimensions 0.450 × 0.450 × 0.003 m) has been provided, on which the pole could be placed in good conditions (Figure 5). A layer of paste with high thermal conduction properties (heat-sink compounds Hy410, with thermal conductivity $\lambda > 1.42$ W/m·K) was applied between the cylindrical support of the mast and the intermediate plate, identical to that used to fix the PTs on structure.

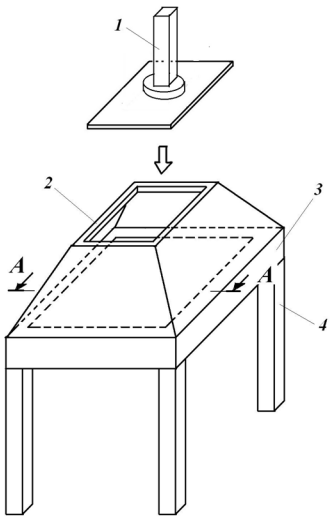

Figure 5. Heating stand, together with the tested pillar model [12].

In the present paper, the effects of heating the column at the base on the propagation of the thermal field along it are analyzed. According to Figure 5, the structural element ***1***, together with the stainless-steel plate fixed to its base, after a translation along the arrow, will be placed on the upper area of the dome in the form of a pyramid trunk **2**, which in turn rests on rigid frame ***3*** and support legs ***4***.

During the experimental investigations, the free surface of the laying plate is covered with such a thermal insulation blanket (Figure 6). The image with the set of 12 Silite bars during operation is shown in Figure 7.

Figure 6. Heating stand, together with the thermal protection enclosure of the column [12].

Figure 7. Silite bars during operation [12].

As an illustration of the efficiency of thermal insulation, it can be mentioned that at the nominal heating temperature $t_{0,\,nom} = 500$ °C of the tested structural elements, the temperature around the support frame ***3*** and the pyramid trunk **2** did not exceed $(45 \ldots 50)$ °C.

The authors designed an original electronic control and adjustment system, presented in the paper [12], which ensured optimal operation in a wide range of dissipated power, as well as accurate monitoring of electricity consumed for heating. Thus, at the nominal value of the supply voltage, the heating system ensures a power of approx. 25 kW, as well

as reaching temperatures $t_{0,\,nom} = (500 \ldots 600)^{\circ}C$ at the base of the structural element under test.

The protocol of the experimental investigations was as follows:

- Placing the structural element ***1*** on the assembled stand, by interposing between them a segment of thermal insulating mattress on the effective placement area (effective contact area), in order to ensure a perfect contact without thermal losses (Figure 6);
- Mounting, on the lower plate of the tested structural element as close as possible to their junction area, a thermocouple type *K*, which will be connected to the temperature controller ATR121B, in order to monitor the desired nominal temperature at the base of the structural element;
- Mounting on the tested structural element all the thermoresistors type PT 100-402 at the level of the dimensions, according to those specified above;
- Connecting these thermoresistors to the data acquisition system;
- Checking the proper operation of all thermoresistors, as well as the type *K* thermocouple;
- Selection of the nominal temperature $t_{0,\,nom}$ and the heating stage;
- Connecting the heating installation to the 380 V power supply;
- Starting the installation with the help of the main switch;
- Monitoring the achievement of the stabilized nominal temperature $t_{0,\,nom}$ with the help of the data acquisition system,
- Additional recording, at the thermal level of the stabilized regime, of the consumed electricity $E_{0,total}\ [kWh]$, as well as of the time $\tau_{0,total}\ [s]$ necessary to reach this regime;
- Repeating the previous steps in order to reach all the nominal temperatures of $t_{0,\,nom} = (100,\ 200,\ 300,\ 400,\ 450,\ 500)\ ^{\circ}C$.
- Some observations can be made:
- The ATR121B temperature controller also has the self-learning function; practically, after the first cycle of reaching the nominal temperature $t_{0,\,nom}$, it will ensure the temperature regulation within very determined limits. Thus, for example, based on the measurements performed at one $t_{0,\,nom} = 500\ ^{\circ}C$, the thermal oscillations related to the adjustment were of maximum $(4 \ldots 5)\ ^{\circ}C$;
- A stabilized temperature regime was considered to be achieved when at the level of the last thermoresistance PT 100-402 (near the upper part of the tested structural element) and the maximum temperature oscillations $(0.2 \ldots 0.3)\ ^{\circ}C$ were observed for a minimum period of $(120 \ldots 180)\ s$.

3. Experimental Results

In the following section, the results obtained on the column provided with four beams in the non-thermally protected version (unpainted with intumescent paint) will be presented. In Figures 8–10, the thermal fields at the level of the column in the stabilized operating regime, the evolution in time of the thermal regimes, and the changes in the ambient temperature and inside the column temperature are shown, in the cases of the elements not covered with thermal paint.

In Figure 8, the horizontal axis refers to the length of the pole, and the vertical one to the imposed temperatures and their evolution along the pole at the level of the nine PTs (thermo-resistances), each marked by the characteristic points of the diagrams; the seven curves T1 ... T7 refer to the imposed temperatures.

Figure 9 shows the variation curves of the temperatures at the level of the nine PTs in relation to the duration of the tests; in addition to the color codes, the coordinates of these thermoresistances are also mentioned.

Figure 10 shows the variation curves of the temperatures: First at the level of the three PTs arranged inside the pillar (Tst.int1 ... 3), second at the level of the one that monitored ambient temperatures (Tamb) and third at three other thermoresistances: at the base of the pillar $z(0)$, the next $z(1)$, and respectively from the top of the pillar $z(9)$, in relation to the time of the tests.

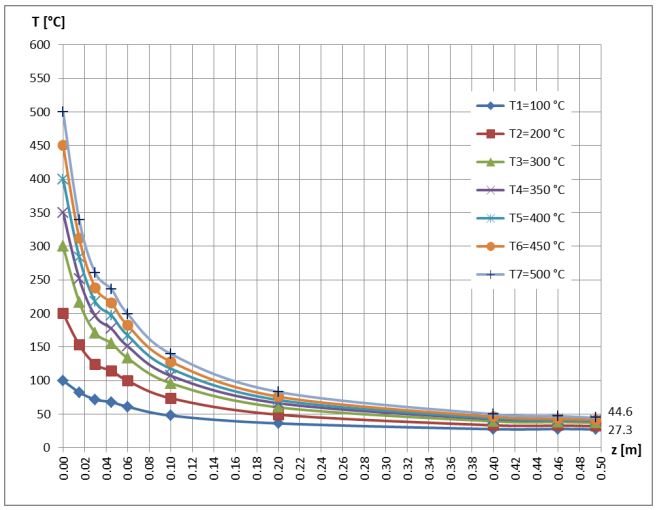

Figure 8. Temperature variation along the pillar in stabilized operating mode.

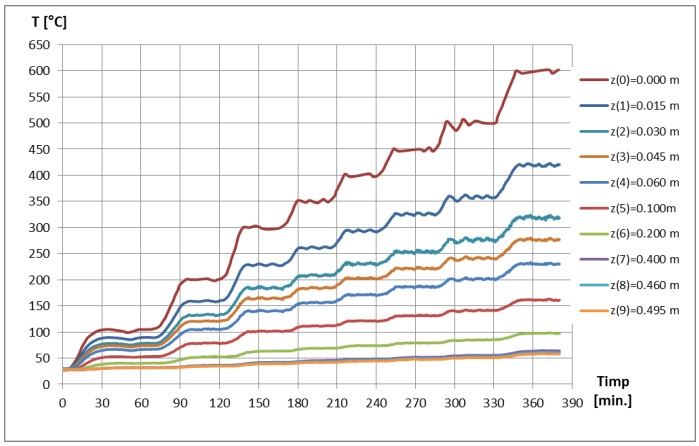

Figure 9. The evolution versus time of the temperature of the unpainted pillar, provided with four beams.

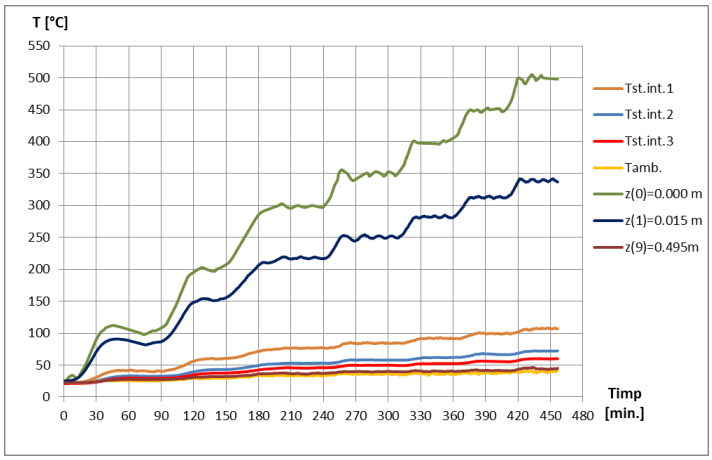

Figure 10. The evolution versus time of the air temperatures inside the unpainted pillar provided with four beams ($T_{st.int}$ 1, 2, 3) of the environment (T_{amb}).

The exponential law of temperature propagation along a straight, full-section bar is well-known [1–3]:

$$T_r(z) = T(z) - T_a = c_1 \cdot e^{m_0 \cdot z} + c_2 \cdot e^{-m_0 \cdot z} \quad (1)$$

where:

T_r [°C] represents the relative temperature, i.e., the difference between the temperature of the bar $T(z)$ and that of the environment T_a;

c_1, c_2 [°C]—integration constants;

$$m_0 = \sqrt{\frac{P}{A} \cdot \frac{\alpha_n}{\lambda}} \left[\frac{1}{m}\right] - \text{parameter;} \quad (2)$$

e—the basis of the natural logarithm;

z $[m]$—the coordinate of the investigated section of the bar, measured from its base;

P $[m]$—the perimeter of the cross section of the bar;

A $[m^2]$—cross-sectional area;

α_n $\left[\frac{W}{m^2 \cdot °C}\right]$—the convection heat transfer coefficient for the outer surface of the bar;

λ $\left[\frac{W}{m \cdot °C}\right]$—the thermal conductivity (coefficient of thermal conductivity) of the bar material.

The generally accepted parameter m_0 is also used in establishing by experiment the size of the heat transfer coefficient α_n, for which it becomes important to establish it as simple, accurate and as safe as possible. In this sense, the methodology developed in [12], based on a polynomial approach instead of the classical, exponential one, is particularly efficient.

The hypothesis $m_0 = const.$ along the entire bar is valid only in the case of bars with the full section. Taking the previous results obtained in [12,27,32,33] into account by which, on the basis of rigorous experimental investigations, it was established that the exponential law of well-known distribution (5) of temperature from solid bars cannot be applied to tubular ones, it results that the condition $m_0 = const.$ is valid only at short intervals.

In the latter case, instead of a single exponential law of the type (5), and therefore of a single condition $m_0 = const.$, at least three intervals must be delimited on the total length of the bar L $[m]$, with exponential laws (and at the same time with val m_0) differing: $z_I \in [0 \div 6] \cdot L$ [%] ; $z_{II} \in [6 \div 12] \cdot L$ [%] ; $z_{III} \in [12 \div 100] \cdot L$ [%] .

Consequently, in the present case, this division led to $z_I \in [0 \div 0.03]$ $[m]$; $z_{II} \in [0.03 \div 0.06]$ $[m]$; and $z_{III} \in [0.06 \div 0.50]$ $[m]$, thus making it possible to accurately approximate these curves by polynomial functions with a relatively small degree.

These new intervals are shown in Figure 11a–c. At first glance, the curves in Figure 11c seem to show strong gradients of temperature variation, but if we look closely at the $z(m)$ scale, it is found that, in fact, these lengths are much larger than in the first two sets of diagrams, resulting in very smooth changes in temperatures per portion $z_{III} \in [0.06 \div 0.50]$ $[m]$.

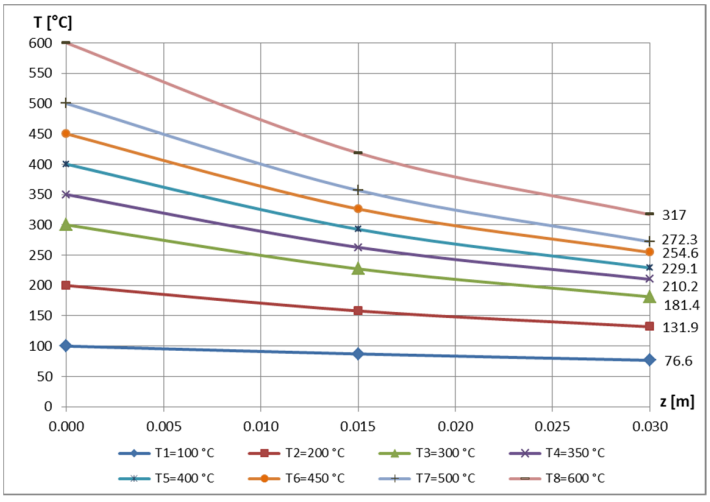

(**a**)

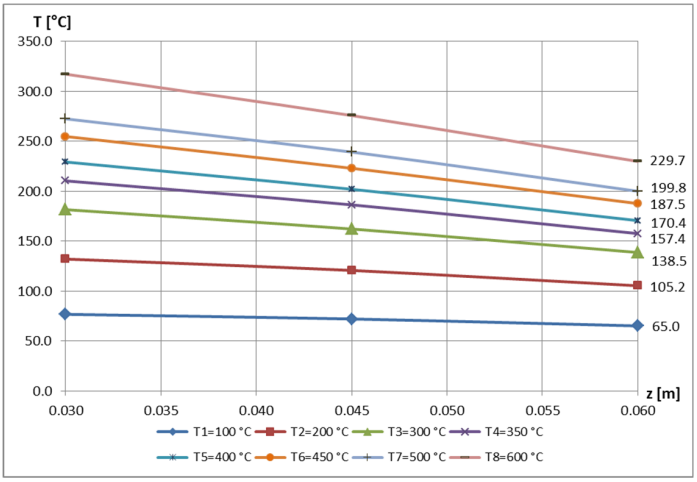

(**b**)

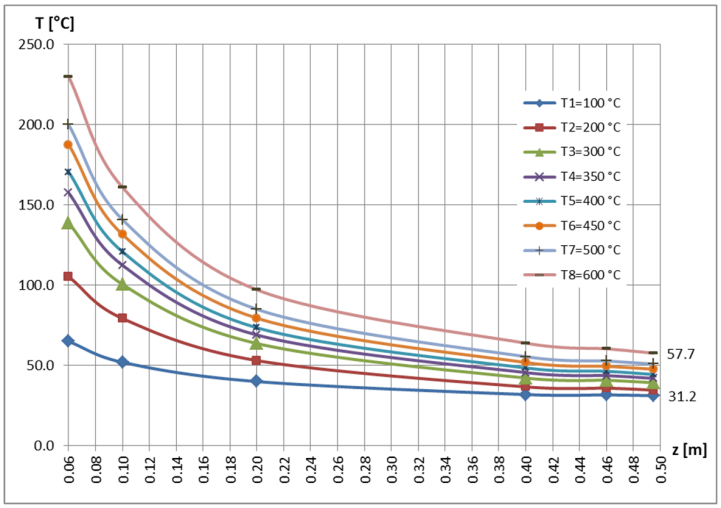

(**c**)

Figure 11. Temperature variation along the intervals of the unpainted column: (**a**) z_I; (**b**) z_{II}; (**c**) z_{III}. (see Figure 8).

Figure 12 shows the variation, with a small gradient, of the thermal fields along a beam.

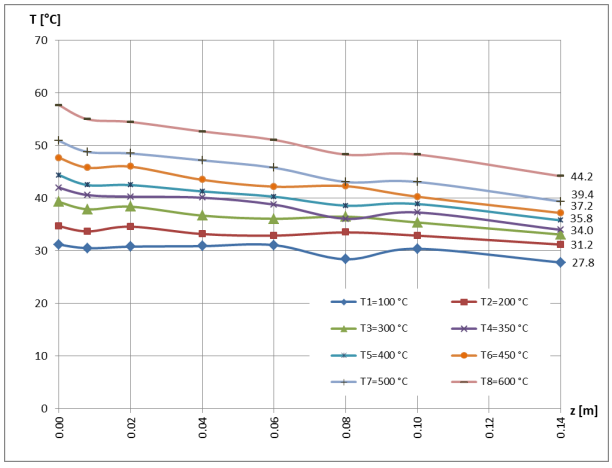

Figure 12. Temperature variation along a thermally unprotected beam.

4. CFD Simulation/Numerical Solution

A three-dimensional numerical model was built to investigate the temperature distribution on the above-described frame. The numerical approach with the commercial software package ANSYS Fluent was applied, based on the Finite Volume Method (FVM).

The temperature at the bottom of the support column is known from the heating performance and measurements, so the circular heating was not modelled.

At the bottom of the column, a constant nominal temperature was prescribed (T = 100; 200; 300; 350; 400; 500 °C).

On the surface of the frame, the standard no-slip condition was used for the velocity. Natural convection develops in the closed domain around the column; a flow can be induced due to the force of gravity acting on the density variations [34]. The ambient air temperature is prescribed based on the experimental data from Figure 10, while the maximum heating temperature of the frame is 500 °C. The Boussinesq model should not be used if the temperature differences in the domain are large [32], so fluid density must be specified as a function of temperature. The fluid properties such as viscosity, density and thermal conductivity were treated as temperature-dependent using polynomial functions. The coefficients of the functions were obtained by fitting the data of VDI-Wärmeatlas [31] in the range 0 °C $\leq T \leq$ 600 °C:

- Density:

$$\rho(T) = 2.4551 - 0.005334T + 5.7033{\cdot}10^{-6}T^2 - 2.3297{\cdot}10^{-9}T^3; \quad (3)$$

- Thermal conductivity:

$$\lambda(T) = 0.0042853 + 7.8292{\cdot}10^{-5}T - 1.4695{\cdot}10^{-8}T^2; \quad (4)$$

The dependence of the viscosity on temperature is given by Sutherland's formula [31]. The external insulation is 0.025 m-thick Fiberfrax Durablanket, the density of which is 128 kg/m^3, while its thermal conductivity depends on the temperature:

$$\lambda(T) = 0.073965 - 2.3719{\cdot}10^{-4}T + 4.2045{\cdot}10^{-7}T^2; \quad (5)$$

In the computational domain, hexagonal elements were used. It can be seen in Figure 13 that the cells are logarithmically spaced, providing a fine grid scale near the solid bodies (frame and insulations) and relatively coarse grid in the far field.

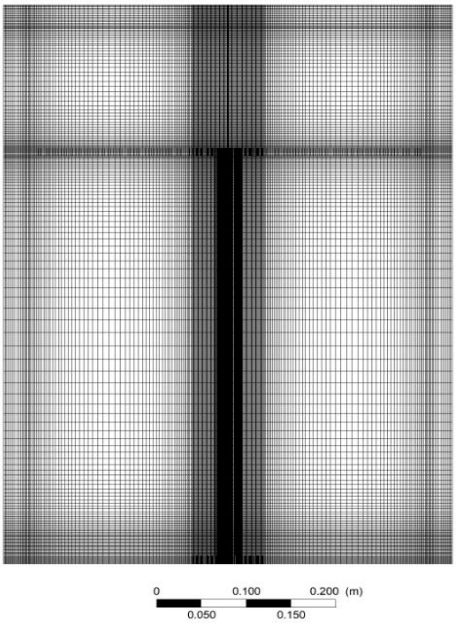

Figure 13. The mesh of the column with four beams.

Two types of mesh were created, i.e., a coarser mesh with approximately 5.66 million cells and a finer mesh with roughly 11.6 million cells. For the two different mesh designs, the temperature values were compared on the column at a height of $z = 0.495$ m at heating temperatures of 500 °C. There was a relative error of about 6% between the two mesh designs.

The obtained values were compared to the measured values, and it is found that the coarser mesh is not suitable for determining the exact values, as there was a difference of almost 9%, while the difference for the finer mesh was 3%.

Therefore, further calculations were performed on the finer mesh, although the calculation time thus increased by several hours.

The governing equations with the boundary conditions are solved using Finite Volume Method. The SIMPLE (Semi-Implicit Method for Pressure-Linked Equation) algorithm was used for pressure–velocity coupling. The second order upwind scheme was used in momentum and energy equations. The calculi included the effect of the internal heat-flux during the heating of the column.

The measurement and calculation results are compared for different heating conditions. Figure 14 shows the temperature distribution along the column, where the measurement results are denoted by EM = experimental measurement, while the numerical values are denoted by CFD = computational fluid dynamics.

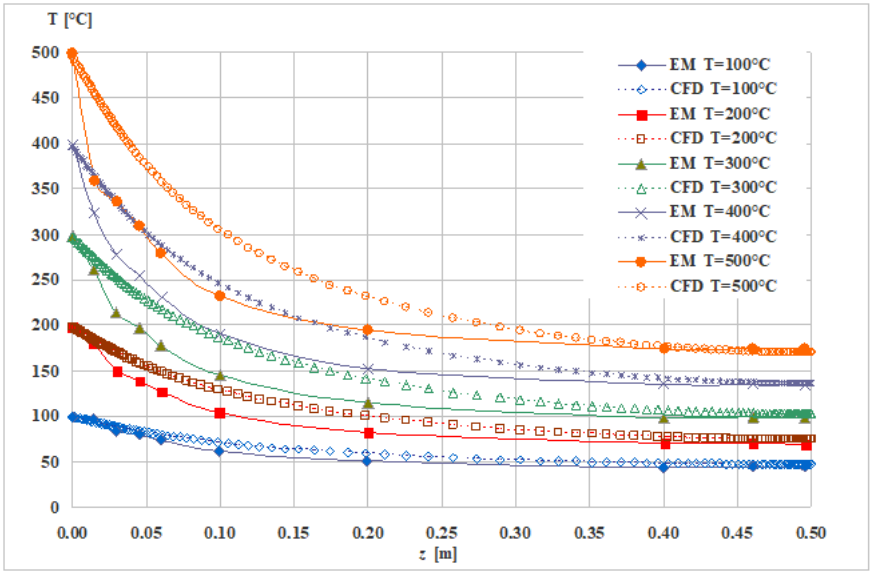

Figure 14. Temperature distribution along the column at different heat power.

At the top of the column, the measurement temperature values agree well with numerical data, but the distribution in the column, i.e., the slope of the curve fitted to the measured and calculated values, differs from each other.

In order to evaluate the obtained differences between experiments and calculi, one can put in evidence the following:

- The thermal radiation was neglected in the calculation;
- It was quite difficult to reproduce the exact environmental conditions from experiments during the simulation;
- The specific case of the hole beams from the $m_0 = const.$ condition (see Equation (5)) must be studied, where, instead of a single domain, the length of the beam has to be divided into three subdomains;
- This last demand was not realized due to the software's particularities and consequently, in the authors' opinion, this can be the main influence factor on the curves' differences.

Distributions of temperature and velocity in the middle plane of the column at 100, 300 and 500 °C are shown in Figure 15. It can be seen that the flow velocity increases along the hot column and flows upwards, and then it hits the insulation on top and the flow continues to spread downwards along the side insulation.

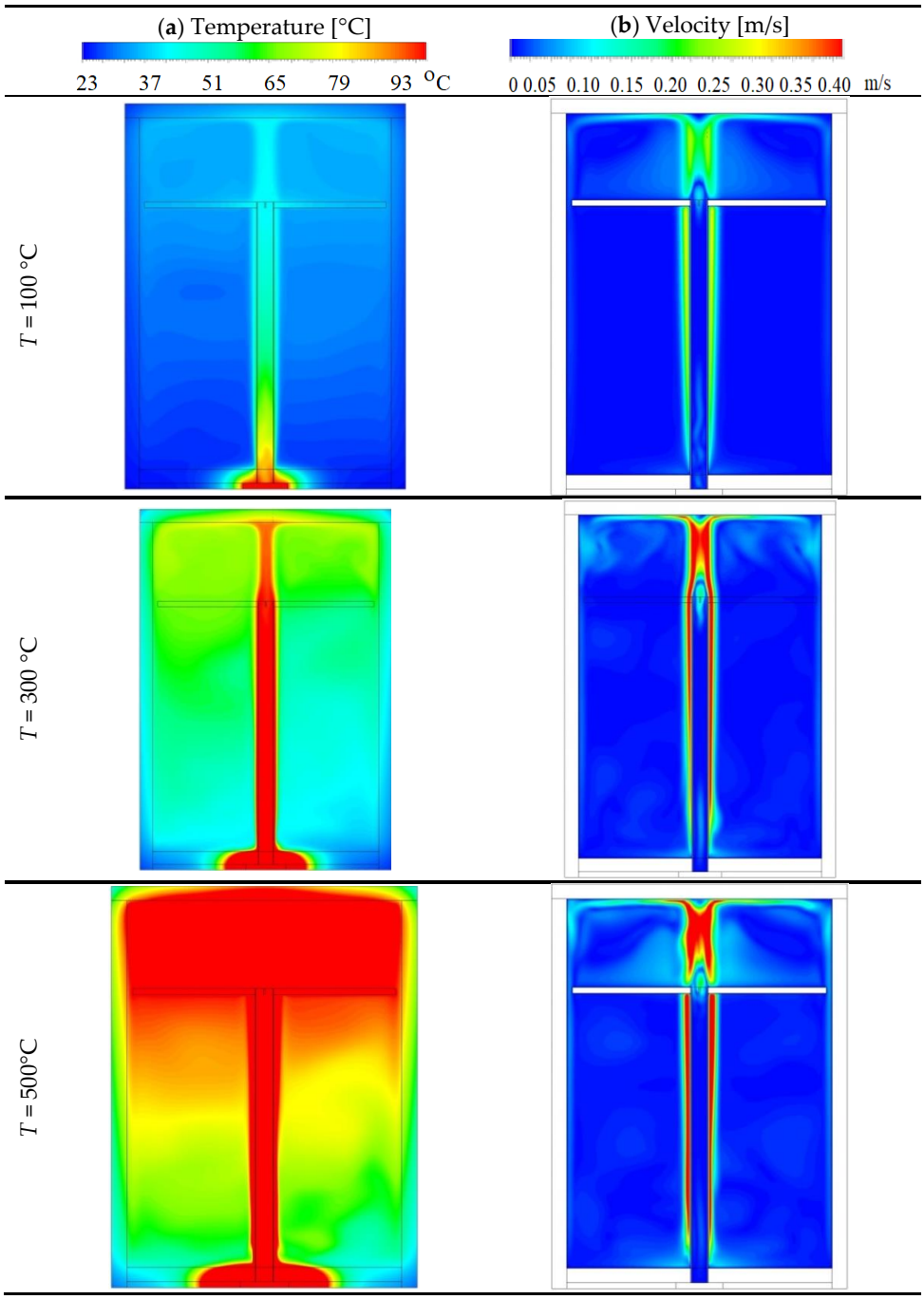

Figure 15. (**a**)Temperature and (**b**) velocity distribution in the middle plane of the frame at 100, 300 and 500 °C.

5. Conclusions

- In the paper, experimental investigations were performed on a reduced model at a scale of 1:10 of a pillar supporting an industrial hall, applying the method of reverse heating;
- A high-power electrical stand was designed, built and tested, with verified performances on a prototype (pillar segment on a natural scale), detailed in the paper [13];

- The numerical simulation of the heating phenomenon of the model was also performed, considering a thermal insulation cylinder, which delimits the space of the model from the environment;
- The obtained differences between the measured values and those from the numerical analysis may be mainly due to the fact that the software could not directly take into account the anomaly valid only on the sub-intervals of the tubular bar compared to the generally valid one (along the entire bar) from those of full sections.
- Among the goals for the near future of the authors are, among others:
    - Improvement of the numerical method, in order to be able to recognize these intervals ($z_I \in [0 \div 6]\cdot L$ [%] ; $z_{II} \in [6 \div 12]\cdot L$ [%] ; $z_{III} \in [12 \div 100]\cdot L$ [%]) from the tubular bars;
    - Validation of numerical models, ensuring obtaining results with a better precision of the measurement results;
    - Improvement of experimental and numerical investigations on bars covered with intumescent paint (so thermally protected).

Author Contributions: Conceptualization, R.-I.S., B.B., P.B., K.J., I.S., G.P., Z.A. and S.V. methodology, P.B., K.J. and I.S.; software, G.P. and Z.A.; validation, R.-I.S., B.B., P.B., K.J., I.S., G.P., Z.A. and S.V.; formal analysis, P.B., K.J. and I.S.; investigation, R.-I.S., I.S., B.B., G.P. and Z.A.; resources, I.S.; data curation, R.-I.S. and I.S.; writing—original draft preparation, I.S.; writing—review and editing, I.S. and S.V.; visualization, R.-I.S., I.S., B.B., G.P., Z.A. and S.V.; supervision, I.S. and K.J.; project administration, I.S.; funding acquisition, I.S. and S.V. All authors have read and agreed to the published version of the manuscript.

Funding: This research received no external funding. The APC was funded by Transilvania University of Brasov.

Institutional Review Board Statement: Not applicable.

Informed Consent Statement: Not applicable.

Data Availability Statement: Not applicable.

Conflicts of Interest: The authors declare no conflict of interest.

Nomenclature

a	Thermal diffusivity (m^2/s);
A	Area (m^2);
Bi	Biot number;
c_p	Constant-pressure specific heat (J/(°C kg));
C	Heat capacity (J/°C);
F	Force (N);
F_o	Fourier number;
g	Gravitational acceleration (m/s^2);
Gr	Grashof number;
l, L	Length (m);
Nu	Nusselt number;
P	Perimeter (m);
Pe	Péclet number;
Pr	Prandtl number;
Q	Heat (J)
$\dot{Q}$	Heat rate (W);
Re	Reynolds number;
St	Stanton number;
t, T	Temperature (°C);
V	Volume (m^3);
w	Velocity (m/s);
$S_{\dot{Q}}$, S_{L_z} , $S_{\Delta t}$, S_τ , $S_{\lambda_{x\ steel}}$, S_ς	Scale factor corresponding to the sizes indicated in the index.

Greek symbols

α	Convection heat transfer coefficient (W/(m^2 °C));
β	Coefficient of volume expansion (°C)$^{-1}$;
δ	Thickness (m);
Δ	Variation;
η	Dynamic viscosity (kg/ms);
λ	Thermal conductivity (W/(m °C));
ν	Kinematic viscosity (m^2/s);
ρ	Density (kg/m^3);
ς	Shape factor (m^{-1});
τ	Time, shear stress (s, N/m^2);
∇	Nabla operator.

Subscripts

x, y, z	Directions.

Appendix A

MDA does not require deep knowledge on the studied phenomenon, but only the knowledge of the variables, which can influence the phenomenon and their dimensions, hereinafter referred to as fundamental dimensions. From the variables thus selected, the so-called Dimensional Matrix (B-A) is formed, where the variables are written on the columns, and their dimensions in rows. In this systematization, the following basic criteria must be taken into account:

- The variables, called main variables, together with their dimensions, called main dimensions, will constitute the matrix A (an invertible quadratic matrix, therefore non-singular, i.e., with $\det|A| \neq 0$); it is clear that two or more identical dimensions should not be found among the main variables, as the condition of non-singleness would be compromised;
- These variables in matrix A must be closely related to the experimental measurements performed on the model;
- The main variables, through the advantages offered by *MDA*, must lead to obtaining a model as simple and flexible as possible, so that the experimental measurements are as safe as possible, accurate, simple and, last but not least, perfectly reproducible;
- The rest of the variables, called auxiliary variables, will form the matrix B, which must not be square, and among them can be found two or more having identical dimensions, without compromising the protocol developed by Szirtes in the works [10,11];
- The order of placement of the variables inside the matrices A and B is not restricted, remaining at the discretion of the user;
- This Dimensional Matrix competes with the matrix $C = -\left(A^{-1} \cdot B\right)^T$, with a unit matrix of order n, and adequate $D \equiv I_{nxn}$, obtaining the so-called dimensional set [7–11], rendered in Equation (A1);

As many rows as the main dimensions $k = N_d$ that have remained after defining matrix A	1. 2. 3. 4. … k.	B	A
As many rows as the n columns (dependent variables) of matrix B; the number of these rows will be identical with that of the resulting dimensionless quantities, π_j $j = 1, 2, \ldots, n$	1. 2. 3. 4. … … n.	$D \equiv I_{nxn}$	$C = -\left(A^{-1} \cdot B\right)^T$

(A1)

The lines related to the D-C matrices offer in a unique, simple and safe way the elements of the Model Law. Another great advantage of *MDA* is that if a variable is either physically or dimensionally insignificant [10,11], it can be removed automatically without the *ML* to undergo significant changes (in essence) regarding the characterization of the studied phenomenon. *MDA* allows the obtaining of the complete set of dimensionless variables, which will constitute the *ML*. It is a very flexible method, allowing disregarding some variables, compared to the general case previously developed; thus, for a particular set of measurements, where the operating conditions of the prototype and the model coincide, certain variables can be excluded from the model law, without affecting the rest of the elements already deduced, because their scale factors (see below) are equal to unity.

The set of relations contained in the *ML* does not represent computational relations in the usual sense, but only firm correlations established between the scale factors $\left(S_{E_j} = \frac{E_{j,\,m}}{E_{j,\,p}}\right)$ of the variables involved, $E_{j,\,m}$, $E_{j,\,p}$, in describing the analyzed phenomenon, where the m index always refers to the model and the p to the prototype.

Thus, each element of the *DS* (see Equation (A1)) represents an exponent, namely: in cases *A* and *B* there are the exponents of the basic dimensions involved, while in *D* and *C* they are of the variables involved.

Consider, for example, *DS*, with 6 basic dimensions $(r_1\ ,\ r_2\ ,\ \ldots\ ,\ r_6)$ and 14 variables involved $(E_1,\ E_2,\ E_3,\ \ldots,\ E_{14})$, given below in the following image. The calculations for matrices *C* and *D* showed the form below *DS*.

How to obtain the fifth element of the *ML* is presented below. This element is related to the connection of the variables E_5 from the prototype and model through the line related to the dimensionless variable π_5, marked in green, i.e., the line π_5 elements, in correlation with the column related to the variable E_5.

	E_1	E_2	E_3	E_4	E_5	E_6	E_7	E_8	E_9	E_{10}	E_{11}	E_{12}	E_{13}	E_{14}
r_1														
r_2														
r_3					***Matricea B***						***Matricea A***			
r_4														
r_5														
r_6														
π_1	1	0	0	0	0	0	0	0	a_1	b_1	c_1	d_1	e_1	f_1
π_2	0	1	0	0	0	0	0	0						
π_3	0	0	1	0	0	0	0	0						
π_4	0	0	0	1	0	0	0	0						
π_5	0	0	0	0	1	0	0	0	a_5	b_5	c_5	d_5	e_5	f_5
π_6	0	0	0	0	0	1	0	0						
π_7	0	0	0	0	0	0	1	0						
π_8	0	0	0	0	0	0	0	1	a_8	b_8	c_8	d_8	e_8	f_8

;

Matrix D ***Matrix C***

The exponents of the independent variables involved $(E_9, \ \dots \ , E_{14})$, i.e., $(a_5 \ , \ \dots \ , \ f_5)$, as well as of the dependent one (E_5), i.e., 1, being on the main diagonal of the matrix D, provide the primary connection relation:

$$\pi_5 = (E_5)^1 \cdot (E_9)^{a_5} \cdot (E_{10})^{b_5} \cdot (E_{11})^{C_5} \cdot (E_{12})^{d_5} \cdot (E_{13})^{e_5} \cdot (E_{14})^{f_5} \tag{A2}$$

It should be noted that some of the exponents $(a_5 \ , \ \dots \ , \ f_5)$ are positive and others are negative. This relation, according to the works [10,11], is equal to the unit, subsequently being expressed the dependent variable involved E_5:

$$\begin{aligned} \pi_5 = (E_5)^1 \cdot (E_9)^{a_5} \cdot (E_{10})^{b_5} \cdot (E_{11})^{c_5} \cdot (E_{12})^{d_5} \cdot (E_{13})^{e_5} \cdot (E_{14})^{f_5} = 1 \ \Rightarrow \\ \Rightarrow \ E_5 = \frac{1}{(E_9)^{a_5} \cdot (E_{10})^{b_5} \cdot (E_{11})^{c_5} \cdot (E_{12})^{d_5} \cdot (E_{13})^{e_5} \cdot (E_{14})^{f_5}}. \end{aligned} \tag{A3}$$

By substituting all the variables involved by the afferent scale factors $\left(S_{E_j} = \frac{E_{j,\,m}}{E_{j,\,p}}\right)$, where $E_{j,\,m}$, $E_{j,\,p}$ represent the sizes of the variable E_j afferent to the model and to the prototype, respectively, results in the searched expression from the second line of the relation (A3).

The complete set (here of eight elements) of the Model Law helps us to establish (depending on the dimensions adopted a priori for the prototype) the dimensions of the model, respectively, for the dependent variable of the prototype and its predictable size according to the results of measurements model.

References

1. Schnittger, J.R. Dimensional Analysis in Design. *J. Vib. Accoustic Stress Reliab.* **1988**, *110*, 401–407.
2. Carinena, J.F.; Santander, M. Dimensional Analysis. *Adv. Electron. Electron Phys.* **1988**, *72*, 181–258.
3. Canagaratna, S.G. Is dimensional analysis the best we have to offer. *J. Chem. Educ.* **1993**, *70*, 40–43. [CrossRef]
4. Remillard, W.J. Applying Dimensional Analysis. *Am. J. Phys.* **1983**, *51*, 137–140.
5. Martins, R.D.A. The Origin of Dimensional Analysis. *J. Frankl. Inst.* **1981**, *311*, 331–337.
6. Gibbings, J.C. A Logic of Dimensional Analysis. *J. Phys. A Math. Gen.* **1982**, *15*, 1991–2002.
7. Trif, I.; Asztalos, Z.; Kiss, I.; Élesztos, P.; Száva, I.; Popa, G. Implementation of the Modern Dimensional Analysis in Engineering Problems-Basic Theoretical Layouts. *Ann. Fac. Eng. Hunedoara* **2019**, *17*, 73–76.
8. Száva, I.; Szirtes, T.; Dani, P. An Application of Dimensional Model Theory in The Determination of the Deformation of a Structure. *Eng. Mech.* **2006**, *13*, 31–39.
9. Gálfi, B.-P.; Száva, I.; Șova, D.; Vlase, S. Thermal Scaling of Transient Heat Transfer in a Round Cladded Rod with Modern Dimensional Analysis. *Mathematics* **2021**, *9*, 1875.
10. Szirtes, T. The Fine Art of Modelling, SPAR. *J. Eng. Technol.* **1992**, *1*, 37.
11. Szirtes, T. *Applied Dimensional Analysis and Modelling*; McGraw-Hill: Toronto, ON, Canada, 1998.
12. Munteanu, I.R. Investigation Concerning Temperature Field Propagation along Reduced Scale Modelled Metal Structures. Ph.D. Thesis, Transilvania University of Brasov, Brasov, Romania, 2018.
13. Száva, I.R.; Șova, D.; Dani, P.D.; Élesztős, P.; Száva, I.; Vlase, S. Experimental Validation of Model Heat Transfer in Rectangular Hole Beams Using Modern Dimensional Analysis. *Mathematics* **2022**, *10*, 409. [CrossRef]
14. Levac, M.L.J.; Soliman, H.M.; Ormiston, S.J. Three-dimensional analysis of fluid flow and heat transfer in single- and two-layered micro-channel heat sinks. *Heat Mass Transf.* **2011**, *47*, 1375–1383.
15. Alshqirate, A.A.Z.S.; Tarawneh, M.; Hammad, M. Dimensional Analysis and Empirical Correlations for Heat Transfer and Pressure Drop in Condensation and Evaporation Processes of Flow Inside Micropipes: Case Study with Carbon Dioxide (CO_2). *J. Braz. Soc. Mech. Sci. Eng.* **2012**, *34*, 89–96.
16. Ferro, V. Assessing flow resistance law in vegetated channels by dimensional analysis and self-similarity. *Flow Meas. Instrum.* **2019**, *69*, 101610.
17. Yao, S.; Yan, K.; Lu, S.; Xu, P. Prediction and application of energy absorption characteristics of thinwalled circular tubes based on dimensional analysis. *Thin Walled Struct.* **2018**, *130*, 505–519.
18. Santiago, J.G. *A First Course in Dimensional Analysis*; MIT Press: Cambridge, MA, USA, 2019.
19. Kivade, S.B.; Murthy, C.S.N.; Vardhan, H. The use of Dimensional Analysis and Optimisation of Pneumatic Drilling Operations and Operating Parameters. *J. Inst. Eng. India Ser. D* **2012**, *93*, 31–36.
20. Barlow, M.A. *Dimensional Analysis & Conversion Factors*; WestBow Press: Bloomington, IN, USA, 2018.
21. Khan, M.A.; Shah, I.A.; Rizvi, Z.; Ahmad, J. A numerical study on the validation of hermal formulations towards the behaviours of RC beams. *Mater. Today Proc.* **2019**, *17*, 227–234. Available online: www.materialstoday.com/proceedings (accessed on 1 November 2021).

22. Yen, P.H.; Wang, J.C. Power generation and electrical charge density with temperature effect of alumina nanofluids using dimensional analysis. *Energy Convers. Manag.* **2019**, *186*, 546–555.
23. Dai, S.J.; Zhu, B.C.; Chen, Q. Analysis of bending strength of the rectangular hole honeycomb beam. In *Applied Mechanics and Materials*; Trans Tech Publications Ltd.: Freienbach, Switzerland, 2013; pp. 993–999.
24. Deshwal, P.S.; Nandal, J.S. On Torsion of Rectangular Beams with Holes at the Center. *Indian J. Pure Appl. Math.* **1991**, *22*, 425–438.
25. Aglan, A.A.; Redwood, R.G. Strain-Hardening Analysis of Beams with 2 WEB- Rectangular Holes. *Arab. J. Sci. Eng.* **1987**, *12*, 37–45.
26. Vlase, S.; Nastac, C.; Marin, M.; Mihalcică, M. A Method for the Study of the Vibration of Mechanical Bars Systems with Symmetries. *Acta Tech. Napoc. Ser. Appl. Math. Mech. Eng.* **2017**, *60*, 539–544.
27. Turzó, G.; Száva, I.R.; Gálfi, B.P.; Száva, I.; Vlase, S.; Hota, H. Temperature distribution of the straight bar, fixed into a heated plane surface. *Fire Mater.* **2018**, *42*, 202–212.
28. Han, X.; Sun, X.; Li, G.; Huang, S.; Zhu, P.; Shi, C.; Zhang, T. A Repair Method for Damage in Aluminum Alloy Structures with the Cold Spray Process. *Materials* **2021**, *14*, 6957. [PubMed]
29. Kim, S.; Ryu, S.; Won, J.; Kim, H.S.; Seo, T. 2-Dimensional Dynamic Analysis of Inverted Pendulum Robot With Transformable Wheel for Overcoming Steps. *IEEE Robot. Autom. Lett.* **2022**, *7*, 921–927.
30. Zhang, H.; Wang, B.; Zhang, J. Parametric of dimensional analysis on iron bath gasifier. *Metalurgija* **2022**, *61*, 295–297.
31. Dani, P. Theoretical and Experimental Study of the Effect of Thermal Field Propagation through Multi-Layer Protective Coatings on the State of Stresses and Strains of Metallic Structures. Ph.D. Thesis, Universitatea Transilvania din Brașov, Facultatea de inginerie Mecanică, Brașov, Romania, 2011.
32. 32VDI. *VDI-Wärmeatlas*, 7th ed.; Verein Deutscher Ingenieure: Düsseldorf, Germany, 1994.
33. Turzó, G. Temperature distribution along a straight bar sticking out from a heated plane surface and the heat flow transmitted by this bar (I)-Theoretical Approach. *ANNALS Fac. Eng. Hunedoara Int. J. Eng.* **2016**, *XIV*, 49–53.
34. Șova, D.; Száva, R.I.; Jármai, K.; Száva, I.; Vlase, S. Modern Method to Analyze the Heat Transfer in a Symmetric Metallic Beam with Hole. *Symmetry* **2022**, *14*, 769. [CrossRef]